

On-chip Kerr parametric oscillation with integrated heating for enhanced frequency tuning and control

JORDAN STONE^{1,*}, DARON WESTLY¹, GREGORY MOILLE^{1,2}, AND KARTIK SRINIVASAN^{1,2}

¹Microsystems and Nanotechnology Division, Physical Measurement Laboratory, National Institute of Standards and Technology, Gaithersburg, MD 20899, USA

²Joint Quantum Institute, NIST/University of Maryland, College Park, MD 20742, USA

*jordan.stone@nist.gov

Compiled April 19, 2024

Nonlinear microresonators can convert light from chip-integrated sources into new wavelengths within the visible and near-infrared spectrum. For most applications, such as the interrogation of quantum systems with specific transition wavelengths, tuning the frequency of converted light is critical. Nonetheless, demonstrations of wavelength conversion have mostly overlooked this metric. Here, we apply efficient integrated heaters to tune the idler frequency produced by Kerr optical parametric oscillation in a silicon-nitride microring across a continuous 1.5 terahertz range. Finally, we suppress idler frequency noise between DC and 5 kHz by several orders of magnitude using feedback to the heater drive.

<http://dx.doi.org/10.1364/ao.XX.XXXXXX>

Nonlinear wavelength conversion, including harmonic and sum/difference frequency generation as well as optical parametric oscillation (OPO), in nanophotonic resonators is an energy-efficient way to generate coherent light at useful colors for a myriad of applications [1–6]. In these devices, large resonator quality factors (Q) boost the effective nonlinearity and gain; however, the gain bandwidth is fundamentally constrained by the resonator linewidth. Hence, to tune the output frequency, one must control the resonator mode frequencies. Of course, frequency tunability is an indispensable aspect of laser systems, enabling spectral alignment with other optical systems (e.g., atomic transitions) for spectroscopy, frequency stabilization, and more.

In particular, due to its intrinsic wavelength flexibility and efficiency, OPO based on four-wave mixing (FWM) in Kerr microresonators is being developed to address the visible-to-near-infrared spectrum [7–9]; but without sophisticated means to control the mode spectrum, frequency tuning has been limited to tens of gigahertz and further suffers from mode hopping [9–11], where the signal and idler waves switch to adjacent longitudinal resonator modes instead of being continuously tuned. While mode hopping provides a convenient way to coarsely tune the OPO frequencies [12, 13], it must be suppressed for continuous tuning. Here, we demonstrate Kerr OPO with an unprecedented idler continuous frequency tuning range of 1.5 THz. We leverage two recent advances in nonlinear microresonator technology: integrated heaters for efficient control of

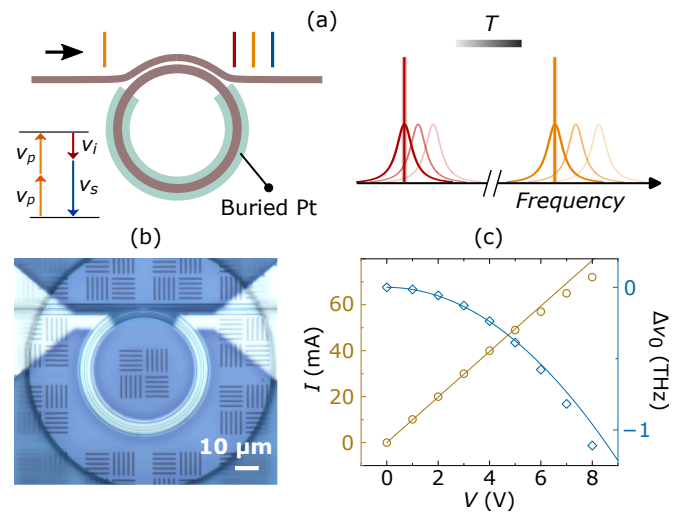


Fig. 1. (a) Illustration of Kerr microresonator optical parametric oscillation (OPO) and its temperature-based frequency control. (Left) Current passing through a buried platinum (Pt) strip generates heat flow to the microring, increasing its temperature, T . (Right) As a result, the microring mode spectrum (illustrated by Lorentzian-shaped curves) is shifted to lower frequencies (light-to-dark curves), along with any resonant lightwaves circulating the device. (b) Device micrograph. (c) Heater current, I (gold circles), and OPO pump mode frequency shift, $\Delta\nu_0$ (blue diamonds), versus the potential difference, V , between the buried heater contacts. Gold and blue curves are linear and quadratic fits to the data, respectively.

the mode spectrum [14, 15], and wavenumber-selective OPO in photonic-crystal microresonators to prevent mode hopping [16]. We show that a targeted frequency deterministically maps to the microresonator temperature, and feedback to the heater drive enables frequency stabilization with in-loop noise reduced by more than six orders of magnitude. Our work explores a new regime of ultra-tunable nonlinear devices that will benefit both $\chi^{(2)}$ and $\chi^{(3)}$ -type light sources.

In our experiments, we pump a silicon nitride (Si_3N_4 , hereafter SiN) photonic-crystal microring near 795 nm. The photonic crystal geometry has recently become a popular and power-

ful design choice for controlling dispersion and enabling novel nonlinear optical phenomena [16–19]. In our test device, the SiN layer thickness, ring outer radius, mean ring width, and ring width modulation amplitude are 450 nm, 25 μm , 820 nm, and 10 nm, respectively. Intracavity FWM converts pump energy into signal and idler waves with widely-separated frequencies, and all three waves are resonant with fundamental transverse electric modes, so that temperature changes which shift the mode spectrum are conveyed to the OPO spectrum, as illustrated in Fig. 1(a). Heat is transferred to the microring by driving current through a platinum (Pt) strip buried in the silicon dioxide (SiO₂) substrate 3 μm below the SiN layer, as shown in Fig. 1(a) and further described in Ref. [14]. Figure 1(b) shows a micrograph of the device used in our experiments. To characterize the heater performance, we measure its resistance and heating efficiency. Specifically, we measure the current flow, I , versus an applied potential difference, V , and we calculate the resistance $R = (100 \pm 1)$ Ohms from a linear fit to these data (see Fig. 1(c)). We also record the pump mode frequency shift, $\Delta\nu_0$, where $\nu_0 \approx 385$ THz, using laser transmission spectroscopy and an optical spectrum analyzer (OSA), and we observe a red-shift of more than 1 THz for the maximum applied voltage.

Our test device oscillates when pumped above its parametric threshold (≈ 30 mW), generating an idler wave near 853 nm with on-chip output power ≈ 2 mW. To examine frequency tuning, we periodically record the OPO spectrum while slowly scanning the pump laser frequency, ν_p , from shorter to longer wavelengths. We repeat this procedure for six different V setpoints and present the optical spectra in Figs. 2(a)–(b). From these spectra, we extract the idler frequencies, ν_i . Notably, for each V setpoint, the range of ν_i values measured during the ν_p scan is more than 200 GHz, which is much greater than the resonator linewidth (≈ 1 GHz). There are two reasons that we can access such a large range without changing V . First, the ν_p scan induces large, dynamically-stable temperature increases which redshift the mode spectrum through the thermo-optic effect [20]. (Hence, ν_i is still being thermally tuned, but the temperature is increased via pump laser absorption rather than dissipated heater current). Second, the idler mode is fixed by the wavenumber-selective frequency matching scheme, so mode hopping does not occur during the ν_p scan. Figure 2(c) shows ν_i and ν_p versus the approximated device temperature, T_{eff} , that we calculate as $T_{\text{eff}} = T_0 + (\nu_p - \nu_0(T_0)) \times d\nu_0/dT$, where T_0 is the ambient temperature, ν_0 is the pump mode frequency at ambient temperature, and $d\nu_0/dT \approx -4.5$ GHz/K is the measured pump mode thermal tuning coefficient. We achieve a continuous (i.e., free of spectral gaps) ν_i tuning range of 1.5 THz using at most ≈ 500 mW of electrical heating power (Fig. 2(b)). The relationship between ν_i and T_{eff} is remarkably linear, indicating their deterministic connection that is enforced by large resonator Q .

In our test device, the Pt electrical leads and resonator are located in different sections of the chip; hence, there is a substantial electrical path length for which dissipated heat is not conducted to the resonator. While in future devices we anticipate increasing the cross-sectional area of the leads to lower their resistance, within the current process, shortening them will improve the heating efficiency. We test this hypothesis by characterizing two more devices and comparing them to the OPO test device (in these additional devices, the dispersion is not suitable to OPO; hence, we cannot directly compare their OPO tuning characteristics). In Fig. 3(a), we present $I - V$ measurements for each device. We find that smaller separations

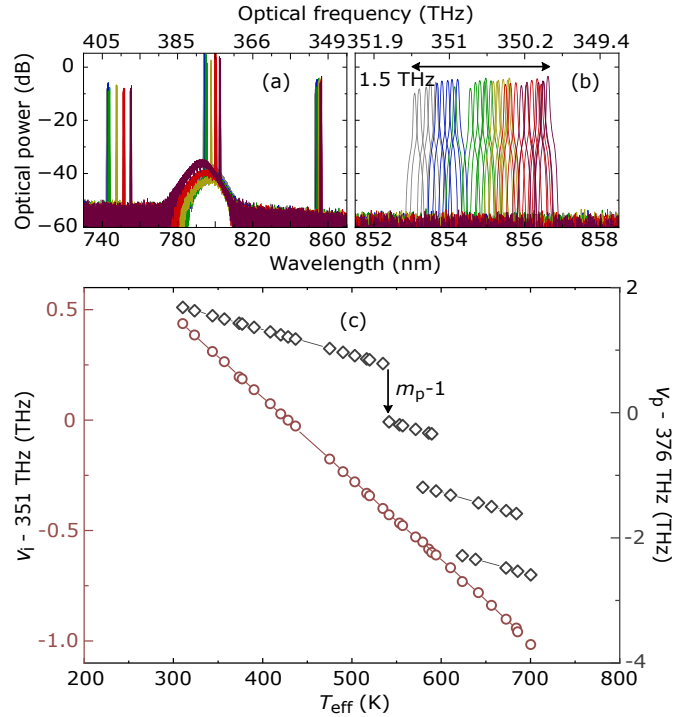


Fig. 2. (a) Compilation of OPO spectra from a single device. The six different colors (more evident in (b)) indicate six different V setpoints: 0, 4, 5, 6, 7, and 8 V (left to right in the spectrum). At each setpoint, the pump laser frequency, ν_p , is scanned through a cavity resonance, and OPO spectra are periodically recorded. Here, 0 dB is referenced to 1 mW. (b) Spectra in (a) zoomed into the idler band. (c) Idler frequency, ν_i , and ν_p (red circles and black diamonds, respectively) versus the estimated device temperature, T_{eff} . Discontinuous jumps in ν_p indicate the pump mode number, m_p , is reduced by one to compensate the temperature-dependent dispersion.

between a microresonator and its electrical leads results in both decreased R and a more nonlinear $I - V$ relationship. Next, we measure $\Delta\nu_0$ versus the electrical heating power for each device and present the results in Fig. 3(b). The device with the smallest resonator-lead separation (blue diamonds) is roughly $2\times$ more efficient than the OPO test device (gold circles).

There are also other factors that determine the OPO tuning efficiency. For instance, the thermal tuning coefficient for a resonator mode with frequency ν_m is $\frac{d\nu_m}{dT} = \frac{\nu_m}{n} \frac{dn}{dT}$, where n is the refractive index and dn/dT is the thermo-optic coefficient. Therefore, although we have chosen to examine ν_i tuning due to the large output power and available analysis tools in the near-infrared, the OPO signal frequency, ν_s , is in general more tunable (such a device would implement wavenumber-selective frequency matching for the signal mode, instead of the idler mode as done here). For example, consider OPO for Na spectroscopy with $\nu_s \approx 589$ nm. For a microresonator geometry similar to our test device, ν_s could be tuned more than 2 THz for the same temperature shifts implied in Fig. 2.

Notably, as T_{eff} is increased, the microring dispersion changes (primarily due to chromatic dispersion of the thermo-optic coefficient) and eventually prevents oscillation when pumping a given mode. However, we compensate by decrementing the pump longitudinal mode number, m_p , by one, as marked in

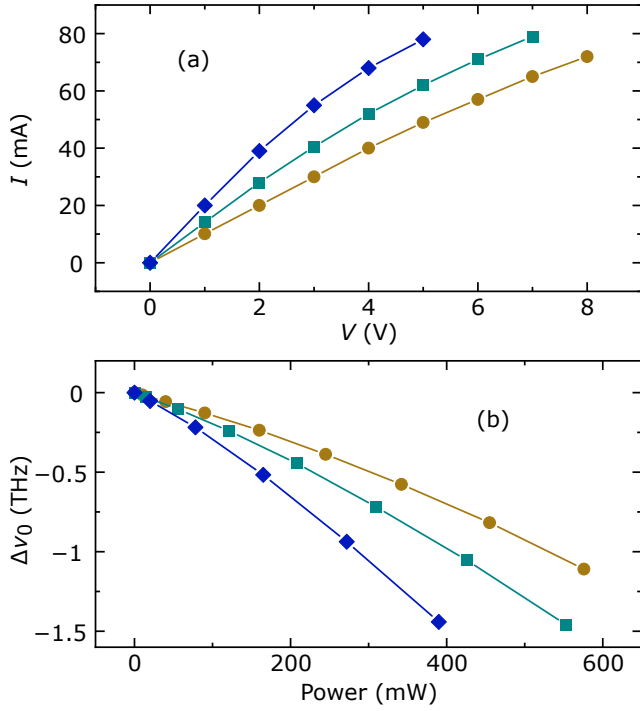


Fig. 3. (a) I versus V for three devices with different separations between the microresonator and heater leads. Device one (gold circles) is our OPO test device and is $\approx 1200 \mu\text{m}$ from its electrical leads, while devices two (green squares) and three (blue diamonds) are $\approx 750 \mu\text{m}$ and $\approx 200 \mu\text{m}$ from their respective leads. The fitted low- V resistance values for devices two and three are (75 ± 1) Ohms and (53 ± 1) Ohms, respectively. (b) $\Delta\nu_0$ versus electrical heating power for the three devices in (a).

Fig. 2(c). In fact, the total ν_i tuning range is limited by the ν_p tuning range (due to decreasing gain of the pump laser amplifier at longer wavelengths); with more ν_p tunability, we expect ν_i could be tuned further. Importantly, the idler mode is fixed by the wavenumber-selective frequency matching scheme [16], so switching m_p does not impact the ν_i tunability (on the other hand, the signal mode number is decreased by two, as seen in Fig. 2(a)). Still, future pump laser integration may confine the range of ν_p values; hence, the ν_i tuning range obtained without m_p adjustments is an important metric. In our experiments, this value is ≈ 820 GHz, which is approaching the ≈ 900 GHz free spectral range of our device, and the corresponding electrical power is 200 mW. We expect that thermally-induced dispersion shifts can be mitigated through advanced dispersion engineering techniques, e.g., by controlling the spatial profiles of microresonator modes to balance thermo-optic dispersion.

Finally, we explore ν_i stabilization through feedback to V . We filter the device output to isolate the idler wave and use a fiber Mach-Zehnder interferometer to transduce ν_i fluctuations into optical power fluctuations that we detect with a transimpedance-amplified photodiode whose output serves as an error signal. In Fig. 4(a), we provide the experimental schematic. The error signal is processed with proportional-integral-derivative control, and we measure its power spectral density using an electronic spectrum analyzer. In Fig. 4(b), we plot the in-loop (i.e., using our error signal monitor) power spectral density of ν_i fluctuations, S_{ii} . Without feedback, the dominant contribution to S_{ii} at

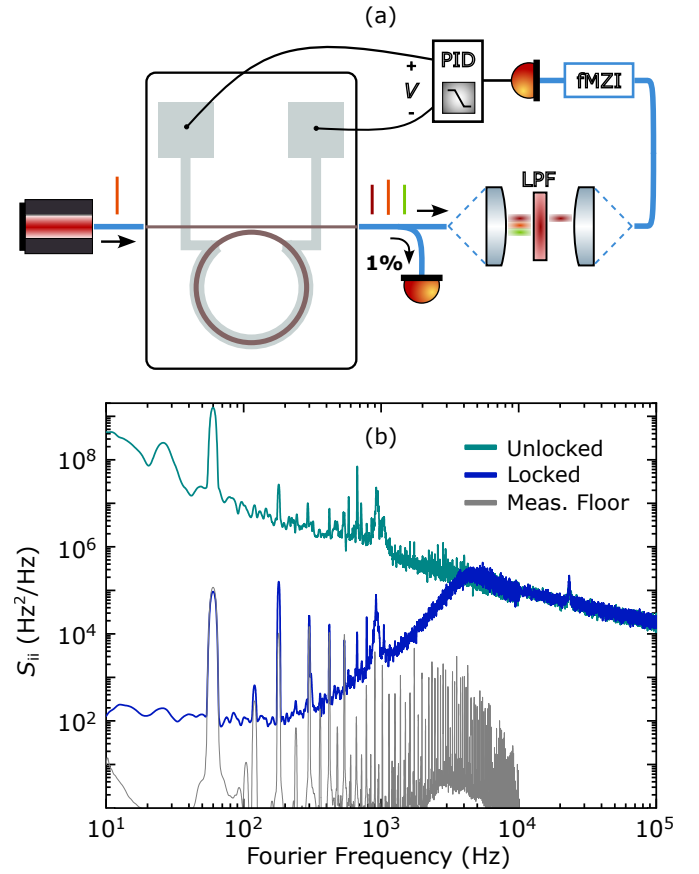


Fig. 4. (a) Experimental schematic for controlling the idler frequency through feedback to the heater drive voltage, V . The output idler wave is coupled from the chip access waveguide into fiber and isolated from the pump and signal waves using a free-space filtering setup. Prior to filtering, one percent of the output light is tapped and detected to monitor the transmitted power. Then, idler frequency fluctuations are transduced to power fluctuations using a fiber-based Mach-Zehnder interferometer (fMZI). Detection of the fMZI output yields an error signal for processing and feedback. LPF: Long-pass filter; PID: Proportional-integral-derivative control. (b) Idler frequency noise spectra with (blue) and without (green) feedback to V . The gray curve indicates the measurement floor.

offset frequencies less than 1 kHz is pump laser frequency noise. Above this frequency, we assess that intrinsic thermorefractive noise plays a large role [21]. With feedback, we reduce S_{ii} by more than six orders of magnitude at low offset frequencies, and we observe noise suppression at offset frequencies up to 5 kHz. Notably, V feedback does not influence ν_p , so ν_i stabilization is enabled for any pump laser technology.

In conclusion, we have used integrated heating to realize efficient and agile frequency control of nonlinear nanophotonics. We experimentally focused on Kerr OPO, where integrated heating dramatically increased the range of continuous frequency tuning to 1.5 THz, and feedback enabled substantial broadband noise reduction. We emphasize that our heating/tuning scheme is broadly applicable to other resonantly-enhanced nonlinear processes, such as harmonic generation. In that context, self-injection-locked microresonators have recently been developed to support full system integration [22–24] and would benefit

from integrated control of the mode spectrum. Finally, we note that our OPO platform exhibits sufficient output power, phase noise, and frequency tunability to replace bulkier light sources holding back the deployment of quantum technologies. Future work will fulfill this mission by developing pump laser- and microelectronics-integrated systems.

Funding. We acknowledge funding support from the DARPA LUMOS and NIST-on-a-chip programs.

Acknowledgments. We are grateful to Dave Long and Oscar Ou for their feedback during manuscript preparation, and we thank Yi Sun for assistance with the micrograph.

Disclosures. DW, GM, and KS have filed a provisional patent application on the buried heater technology used in this work.

Data availability. Data underlying the results presented in this paper may be obtained from the authors upon reasonable request.

REFERENCES

1. X. Guo, C.-L. Zou, and H. X. Tang, *Optica* **3**, 1126 (2016).
2. Z. Hao, J. Wang, S. Ma, *et al.*, *Photonics Res.* **5**, 623 (2017).
3. X. Lu, G. Moille, A. Singh, *et al.*, *Optica* **6**, 1535 (2019).
4. L. Ledezma, A. Roy, L. Costa, *et al.*, *Sci. Adv.* **9**, eadf9711 (2023).
5. J. B. Surya, X. Guo, C.-L. Zou, and H. X. Tang, *Optica* **5**, 103 (2018).
6. J. Lu, A. Al Sayem, Z. Gong, *et al.*, *Optica* **8**, 539 (2021).
7. X. Lu, G. Moille, A. Rao, *et al.*, *Optica* **7**, 1417 (2020).
8. R. R. Domenegueti, Y. Zhao, X. Ji, *et al.*, *Optica* **8**, 316 (2021).
9. N. L. B. Sayson, T. Bi, V. Ng, *et al.*, *Nat. Photonics* **13**, 701 (2019).
10. Y. Tang, Z. Gong, X. Liu, and H. X. Tang, *Opt. Lett.* **45**, 1124 (2020).
11. J. R. Stone, G. Moille, X. Lu, and K. Srinivasan, *Phys. Rev. Appl.* **17**, 024038 (2022).
12. Y. Sun, J. Stone, X. Lu, *et al.*, arXiv preprint arXiv:2401.12823 (2024).
13. D. Pidgayko, A. Tusnin, J. Riemensberger, *et al.*, *Optica* **10**, 1582 (2023).
14. G. Moille, D. Westly, E. F. Perez, *et al.*, *APL Photonics* **7** (2022).
15. E. Nitiss, B. Zabelich, J. Hu, *et al.*, *Opt. Express* **31**, 14442 (2023).
16. J. R. Stone, X. Lu, G. Moille, *et al.*, *Nat. Photonics* pp. 1–8 (2023).
17. J. A. Black, G. Brodnik, H. Liu, *et al.*, *Optica* **9**, 1183 (2022).
18. S.-P. Yu, D. C. Cole, H. Jung, *et al.*, *Nat. Photonics* **15**, 461 (2021).
19. G. Marty, S. Combr e, F. Raineri, and A. De Rossi, *Nat. photonics* **15**, 53 (2021).
20. T. Carmon, L. Yang, and K. J. Vahala, *Opt. express* **12**, 4742 (2004).
21. G. Huang, E. Lucas, J. Liu, *et al.*, *Phys. Rev. A* **99**, 061801 (2019).
22. M. Clementi, E. Nitiss, J. Liu, *et al.*, *Light. Sci. & Appl.* **12**, 296 (2023).
23. J. Ling, J. Staffa, H. Wang, *et al.*, *Laser & Photonics Rev.* p. 2200663 (2023).
24. B. Shen, L. Chang, J. Liu, *et al.*, *Nature* **582**, 365 (2020).

FULL REFERENCES

1. X. Guo, C.-L. Zou, and H. X. Tang, "Second-harmonic generation in aluminum nitride microrings with 2500%/w conversion efficiency," *Optica* **3**, 1126–1131 (2016).
2. Z. Hao, J. Wang, S. Ma, *et al.*, "Sum-frequency generation in on-chip lithium niobate microdisk resonators," *Photonics Res.* **5**, 623–628 (2017).
3. X. Lu, G. Moille, A. Singh, *et al.*, "Milliwatt-threshold visible–telecom optical parametric oscillation using silicon nanophotonics," *Optica* **6**, 1535–1541 (2019).
4. L. Ledezma, A. Roy, L. Costa, *et al.*, "Octave-spanning tunable infrared parametric oscillators in nanophotonics," *Sci. Adv.* **9**, eadf9711 (2023).
5. J. B. Surya, X. Guo, C.-L. Zou, and H. X. Tang, "Efficient third-harmonic generation in composite aluminum nitride/silicon nitride microrings," *Optica* **5**, 103–108 (2018).
6. J. Lu, A. Al Sayem, Z. Gong, *et al.*, "Ultralow-threshold thin-film lithium niobate optical parametric oscillator," *Optica* **8**, 539–544 (2021).
7. X. Lu, G. Moille, A. Rao, *et al.*, "On-chip optical parametric oscillation into the visible: generating red, orange, yellow, and green from a near-infrared pump," *Optica* **7**, 1417–1425 (2020).
8. R. R. Domenegueti, Y. Zhao, X. Ji, *et al.*, "Parametric sideband generation in cmos-compatible oscillators from visible to telecom wavelengths," *Optica* **8**, 316–322 (2021).
9. N. L. B. Sayson, T. Bi, V. Ng, *et al.*, "Octave-spanning tunable parametric oscillation in crystalline kerr microresonators," *Nat. Photonics* **13**, 701–706 (2019).
10. Y. Tang, Z. Gong, X. Liu, and H. X. Tang, "Widely separated optical kerr parametric oscillation in aln microrings," *Opt. Lett.* **45**, 1124–1127 (2020).
11. J. R. Stone, G. Moille, X. Lu, and K. Srinivasan, "Conversion efficiency in kerr-microresonator optical parametric oscillators: From three modes to many modes," *Phys. Rev. Appl.* **17**, 024038 (2022).
12. Y. Sun, J. Stone, X. Lu, *et al.*, "Advancing on-chip kerr optical parametric oscillation towards coherent applications covering the green gap," *arXiv preprint arXiv:2401.12823* (2024).
13. D. Pidgayko, A. Tusnin, J. Riemensberger, *et al.*, "Voltage-tunable optical parametric oscillator with an alternating dispersion dimer integrated on a chip," *Optica* **10**, 1582–1586 (2023).
14. G. Moille, D. Westly, E. F. Perez, *et al.*, "Integrated buried heaters for efficient spectral control of air-clad microresonator frequency combs," *APL Photonics* **7** (2022).
15. E. Nitiss, B. Zabelich, J. Hu, *et al.*, "Tunable photo-induced second-harmonic generation in a mode-engineered silicon nitride microresonator," *Opt. Express* **31**, 14442–14453 (2023).
16. J. R. Stone, X. Lu, G. Moille, *et al.*, "Wavelength-accurate nonlinear conversion through wavenumber selectivity in photonic crystal resonators," *Nat. Photonics* pp. 1–8 (2023).
17. J. A. Black, G. Brodnik, H. Liu, *et al.*, "Optical-parametric oscillation in photonic-crystal ring resonators," *Optica* **9**, 1183–1189 (2022).
18. S.-P. Yu, D. C. Cole, H. Jung, *et al.*, "Spontaneous pulse formation in edgeless photonic crystal resonators," *Nat. Photonics* **15**, 461–467 (2021).
19. G. Marty, S. Combrié, F. Raineri, and A. De Rossi, "Photonic crystal optical parametric oscillator," *Nat. photonics* **15**, 53–58 (2021).
20. T. Carmon, L. Yang, and K. J. Vahala, "Dynamical thermal behavior and thermal self-stability of microcavities," *Opt. express* **12**, 4742–4750 (2004).
21. G. Huang, E. Lucas, J. Liu, *et al.*, "Thermorefractive noise in silicon-nitride microresonators," *Phys. Rev. A* **99**, 061801 (2019).
22. M. Clementi, E. Nitiss, J. Liu, *et al.*, "A chip-scale second-harmonic source via self-injection-locked all-optical poling," *Light. Sci. & Appl.* **12**, 296 (2023).
23. J. Ling, J. Staffa, H. Wang, *et al.*, "Self-injection locked frequency conversion laser," *Laser & Photonics Rev.* p. 2200663 (2023).
24. B. Shen, L. Chang, J. Liu, *et al.*, "Integrated turnkey soliton microcombs," *Nature* **582**, 365–369 (2020).